applied sciences

MDPI

Article

Thermal Conductivity and Convection Heat Transfer Coefficient of Aluminum Cellular Structures Filled with Water and Air

Alessandra Ceci, Paolo Coppa, Sandra Corasaniti, Girolamo Costanza * and Maria Elisa Tata

Industrial Engineering Department, University of Rome Tor Vergata, Via del Politecnico 1, 00133 Rome, Italy; alessandra.ceci@uniroma2.it (A.C.); coppa@uniroma2.it (P.C.); sandra.corasaniti@uniroma2.it (S.C.); elisa.tata@uniroma2.it (M.E.T.)

* Correspondence: costanza@ing.uniroma2.it; Tel.: +39-06-72597185

Abstract

The present study investigates the thermal conductivity (λ) and convective heat transfer coefficient (h) of AA 6082 aluminum cellular structures immersed in water and air using a thermal conductivity probe (TCP) manufactured by the authors. The probe is a cylindrical needle 0.6 mm in diameter (D) and 60 mm in length (L), obtaining an L/D ratio = 100 ratio, which satisfies the infinite line-source assumption and enables discrimination between pure-fluid and composite (fluid + solid) thermal behavior. Cellular samples are manufactured with the Lost-PLA process and tested at temperatures of 5, 20, and 40 °C, feeding the TCP with different currents, under controlled heating conditions. The results show that the presence of the aluminum cellular structure enhances heat transfer compared with that of pure fluids. In air, the effective thermal conductivity is higher by approximately 37–45% than that in pure air, reaching about 0.038 W m^{-1} K^{-1} at higher temperatures. In water, λ increases from approximately 0.8 to 1.2 W m^{-1} K^{-1} over the investigated temperature range, corresponding to an enhancement of about 45–80% compared with that of pure water. Similarly, the convective heat transfer coefficient is higher by about 22–32% in air (h ≈ 38–41 W m^{-2} K^{-1}) and 19–54% in water (up to ~440 W m^{-2} K^{-1}), depending on temperature. These results indicate that the high thermal conductivity of the aluminum skeleton mainly improves conduction ("thermal bridging"), while convection may be locally affected within the pores. This study confirms the capability of the TCP method to discriminate between fluid and composite heat transfer contributions and highlights the potential of additively manufactured aluminum cellular structures for lightweight thermal management applications.

Keywords: aluminum alloys; cellular structures; 3D printing; additive manufacturing; lost PLA; thermal conductivity; convection heat transfer coefficient

Check for updates

Academic Editor: Satoru Okamoto

Received: 14 December 2025
Revised: 24 January 2026
Accepted: 1 February 2026
Published: 3 February 2026

Copyright: © 2026 by the authors. Licensee MDPI, Basel, Switzerland. This article is an open access article distributed under the terms and conditions of the Creative Commons Attribution (CC BY) license.

1. Introduction

In recent decades, metallic cellular structures, such as open-cell foams and topologically complex lattices, has attracted increasing interest for high-efficiency heat transfer applications. The pioneering works of Lu [1] and Calmidi & Mahajan [2] laid the theoretical foundations for forced convection heat transfer in high-porosity metal foams, highlighting the roles of permeability, porosity, and cell interconnectivity. Other subsequent studies [3,4] experimentally investigated the thermal behavior of aluminum foams immersed in air and water as working fluids.

Numerous studies have highlighted the effect of geometric configuration and filling fluid characteristics on the thermal performance of the composite. Mancin et al. [5] conducted extensive research on the thermal performance of aluminum foams, particularly when forced convection was activated. Their work focused on the experimental characterization of the heat transfer and pressure drop in aluminum foams as pore density and porosity varied. They analyzed the influence of these two parameters on the thermal efficiency of the obtained heat exchangers as a result of the enhanced transfer surfaces. Similar findings were reported by Nawaz [6], who combined experiments and numerical simulations to study foams with different pore densities, and by Bayomy and Saghir [7], who examined the heat transfer characteristics of aluminum metal foams subjected to water flow in the steady state with open or close porosity, combining experimental measurements and numerical simulations in order to evaluate the thermal performance of these porous structured. Chen [8] and Xiao [9] contributed to the thermo-fluid dynamic characterization of these kinds of structures under different flow regimes.

In parallel, the advent of additive manufacturing (AM) enabled the production of three-dimensional lattices and Triply Periodic Minimal Surfaces (TPMSs) optimized to maximize heat exchange surfaces. Recent works [10–13] demonstrate how advanced topological design, supported by CFD simulations, can lead to improved performance compared to conventional foams. Maskery [14] further highlighted the advantages of 3D-printed cellular structures in terms of geometric customization and mechanical strength.

Despite the rich theoretical and numerical literature [15–18], the availability of systematic experimental data comparing metal foams and lattices under real operating conditions with air and water as working fluids remains limited. Recent reviews [19,20] emphasize the need for comparative measurements to validate CFD models and define reliable design guidelines. The aim of this work is therefore to contribute to bridging this gap by providing direct experimental measurements of the effective thermal conductivities and convective heat transfer coefficients of aluminum cellular structures saturated with air and water, providing valuable reference data for the design of compact, high-efficiency heat exchangers.

2. Sample Description and Manufacturing

The structures analyzed in this work were made of aluminum alloy AA 6082 and were produced in the authors' laboratory using the Lost-PLA method [21]. This method, similar to the lost-wax casting technique, is based on creating a metal structure starting from a PLA mask manufactured using a 3D printer. Figure 1 illustrates the schematic of the entire Lost-PLA production process.

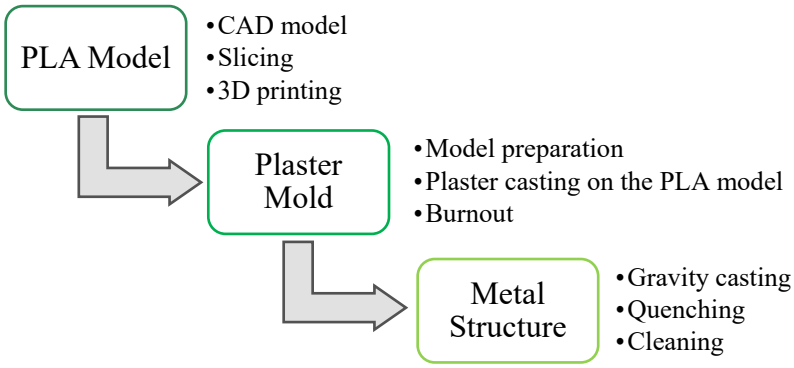

Figure 1. Schematic of the metal structure production process (Lost-PLA).

The fabrication process using the "Lost-PLA" technique begins with defining the lattice geometry in a CAD model. The CAD design stage plays a crucial role in the fabrication of three-dimensional cellular structures with complex geometries. From a structural design

perspective, such cellular structures are generated through the spatial repetition of a base cell. Among the various approaches available for the CAD modeling of cellular structures, the parametric method is one of the most effective, as it allows for the creation of geometries that are both repetitive and easily adjustable.

In the present work, the base cell was defined parametrically: by changing the values of the parameters a and b in Equation (1), different geometric configurations can be obtained, as illustrated in Figure 2 [22].

$$F(x,y,z) = cos(2\pi x) + cos(2\pi y) + cos(2\pi z) + a \cdot [cos(2\pi x) \cdot cos(2\pi y)] + cos(2\pi y) \cdot cos(2\pi z) + cos(2\pi y) \cdot cos(2\pi z) + cos(2\pi z) \cdot cos(2\pi x) + b = 0 \quad (1)$$

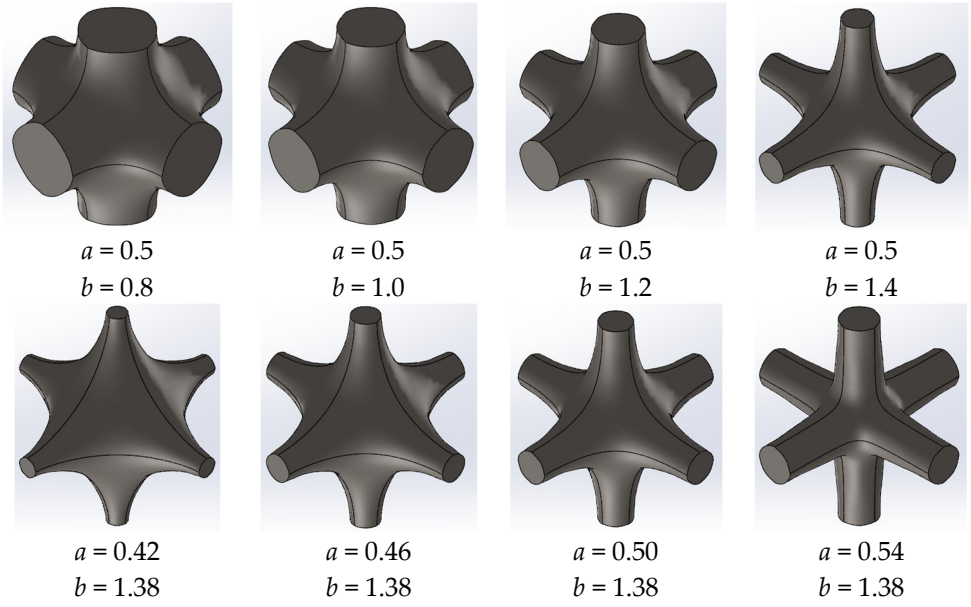

Figure 2. Different geometries of the base cell created by varying the parameters a and b in Equation (1) [22].

The parameters used in the present study were $a = 0.5$ and $b = 0.8$, resulting in a cellular structure with optimized mechanical and thermal properties for the intended application. Figure 3 shows the CAD model of the designed structure obtained through the spatial repetition of the base cell.

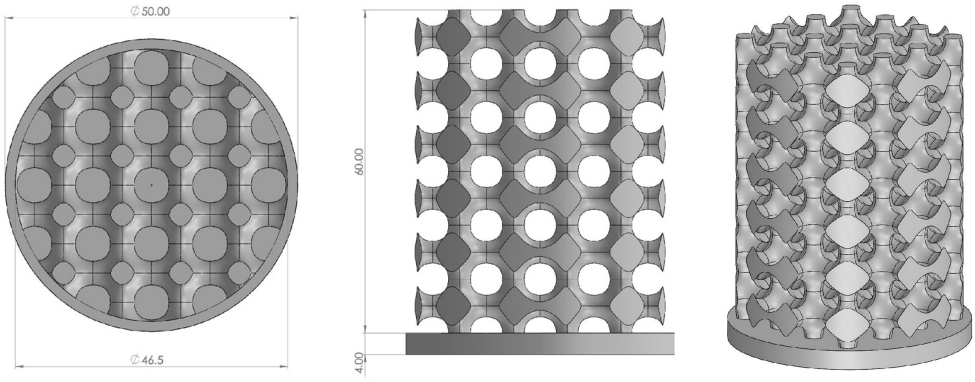

Figure 3. (**a**) Top view, (**b**) front view, and (**c**) isometric view of the CAD model of the structure.

After defining the geometry, the model is exported in STL format and prepared for 3D printing using slicing software. In this step, key print parameters (layer resolution,

print speed, extruder and bed temperatures) are optimized to ensure a precise PLA pattern, see Table 1. The quality of the polymer model is critical: any geometric imperfection will be directly reproduced in the plaster mold and, ultimately, in the final metal structure, potentially affecting its functional performance.

Table 1. Dimensions of the CAD model.

Cell size	$1 \times 1 \times 1$ mm^3
Average structure diameter	$d_s = 4.0$ mm
Equivalent pore diameter	$d_p = 6.0$ mm
Structure	$\varnothing_s = 46.5$ mm $H_s = 60.0$ mm
Basement	$\varnothing_b = 50$ mm $H_b = 5.0$ mm

The characteristic cell size L_c corresponds to the side length of the cube in which the CAD unit cell is inscribed, equal to $10 \times 10 \times 10$ mm^3. In addition to the unit cell size, the characteristic pore dimension was extracted from the CAD model. As shown in Figure 3a,b, the pores have an approximately circular cross-section with an equivalent diameter of about 6 mm. This value is representative of the characteristic fluid passage size within the lattice.

Once the PLA model is printed, venting and pouring channels are added using plastic tubes attached with hot glue. These channels are vital for allowing gases to escape during metal pouring, thus preventing voids and defects. The entire assembly is placed in a heat-resistant container, e.g., a steel cylinder, and fully covered with a special plaster mixture, carefully mixed to avoid air bubbles. Weights or fixtures are used to hold the model steady during plaster assembling and to create clear pathways for the pouring channels. The mold is then completely dried, typically for at least 24 h, to ensure that any residual moisture evaporates and does not cause internal pressure to increase during burnout.

During the burnout stage, the PLA pattern is removed to create the cavity for metal casting. The mold is placed in a muffle furnace and gradually heated from room temperature to approximately 800–900 °C. A controlled temperature increase prevents thermal shock and mold cracking. The PLA melts at about 173 °C and decomposes completely at higher temperatures (about 250 °C). This stage must be carefully monitored to ensure no polymer residue remains inside the mold. The total burnout time depends on the size and complexity of the structure.

Once burnout is completed, AA 6082 aluminum alloy is melted in an electric furnace to a temperature sufficiently above its melting point to maintain high fluidity during pouring. The plaster mold may be preheated to reduce thermal gradients, helping to prevent premature solidification. Controlled mechanical vibrations can be applied during pouring to facilitate complete infiltration of the molten metal into the intricate cavities.

After pouring, the casting is allowed to solidify at room temperature for a sufficient amount of time. It is then quenched by rapid immersion in cold water to enhance the mechanical properties through hardening. Finally, the plaster mold is mechanically removed or washed away, and the metallic structure is cleaned to eliminate any residual plaster and excess metal. Figure 4 shows the steps of the Lost-PLA process, already shown in Figure 1.

Once the final metallic structure is obtained, its geometric properties, such as apparent density and theoretical porosity, are evaluated combining CAD-derived volume and weight data with theoretical models available in the literature.

The apparent density ($\rho*$) and the theoretical porosity (ϕ) of the cellular structure are determined through the Gibson–Ashby model [23], commonly used to describe metallic cellular materials.

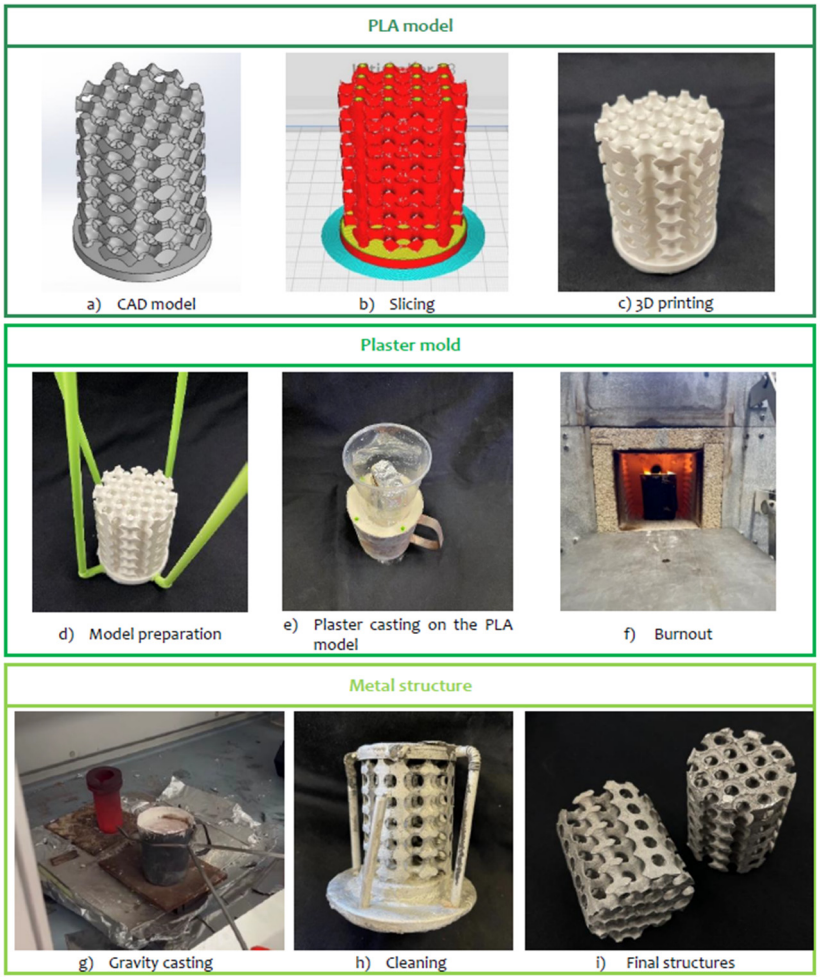

Figure 4. Steps of the Lost-PLA process: (**a**) CAD model, (**b**) slicing, (**c**) 3D printing, (**d**) model preparation, (**e**) plaster casting on the PLA model, (**f**) burnout, (**g**) gravity casting, (**h**) cleaning, (**i**) final structures.

The external volume of the cylindrical configuration, 60 mm high and with a 46.5 mm diameter, is calculated as

$$V_{ext} = \pi \frac{\varnothing_s}{4}^2 H \tag{2}$$

The weight calculated with the CAD model is 90.64 g, yielding an apparent density of

$$\rho^* = \frac{m_{CAD}}{V_{ext}} \tag{3}$$

The relative density is defined as the ratio between the apparent density and the bulk density of the solid material (AA 6082), the latter being $\rho_s = 2.7\ 10^3$ kg/m^3.

Finally, the theoretical porosity is calculated as

$$\Phi = 1 - \frac{\rho^*}{\rho_s} \tag{4}$$

This equation leads to a percentage of voids of 67%, in agreement with what was reported in the literature for TPMS or Kelvin cell geometries [14].

The main geometric and volumetric parameters estimated for the cellular structure with this procedure are summarized in Table 2.

Table 2. Estimated geometric and volumetric parameters.

Parameter	Symbol	Value
Structure diameter	D	46.50 mm
Structure height	h	60.00 mm
External volume	V_{ext}	1.02 10^{-4} m^3
CAD model weight	m_{CAD}	0.09 kg
Bulk material density (AA 6082)	ρ_s	2.70 10^3 kg/m^3
Apparent density	ρ^*	0.89 10^3 kg/m^3
Relative density	ρ^*/ρ_s	0.33
Theoretical porosity	ϕ	0.67

3. Measurement Procedure

3.1. Theoretical Background and Data Reduction

The thermal conductivity of the medium surrounding the probe is obtained from the classical solution of a line heat source embedded in an infinite medium with constant properties λ and α. If a uniform thermal power per unit length $\dot{q}$ (Wm^{-1}) is suddenly applied at $t = 0$, the temperature rise at radial distance r and time t is given by Equation (5) [24]:

$$\Delta T(r,t) = \frac{\dot{q}}{4 \cdot \pi \cdot \lambda}\left[\ln\left(\frac{4 \cdot \alpha \cdot t}{r^2} - \gamma\right)\right] \quad (5)$$

with $\gamma = 0.5772$ (Euler–Mascheroni constant). Hence, the plot of ΔT versus $\ln t$ is linear in a pure conductive regime. The slope of this trend is

$$m = \frac{d(\Delta T)}{d(ln\ t)} = \dot{q}/4\pi\lambda \quad (6)$$

Hence,

$$\lambda = \frac{\dot{q}}{4 \cdot \pi \cdot m} \quad (7)$$

This slope m is computed through a linear regression of all the data during the linear T vs. $\ln t$ trend, also obtaining the uncertainty due to the calculated uncertainty of the slope, from the corresponding element of the covariant matrix of the unknowns. The line heat rate is computed from the electrical power dissipated in the heated wire segment of length L.

$$\dot{q} = \frac{\dot{Q}}{L} = \frac{RI^2}{L} \quad (8)$$

In practice, the conductive window is selected before the onset of free convection, as evidenced by the straight portion of the $\Delta T - \ln t$ curve; the long, slender probe ($L/D \approx 100$) minimizes border effects and supports the infinite-line approximation.

Equation (5) assumes

(i) Radially infinite medium;
(ii) Negligible thermal contact resistance at the probe surface;
(iii) Constant properties of the tested material over the examined ΔT (not influenced by small temperature rises);
(iv) No convection or radiation during the conductive window.

In this test, $\Delta T < 15$–20 °C, so radiation is negligible; the linear window is chosen before the curve departs from linearity due to the start of convection and after the initial region governed by thermal capacity.

After sufficient heating time, the measured temperature difference between the probe and the surrounding medium becomes approximately constant (plateau). In this phase,

the electrical power supplied to the wire is balanced by convective heat transfer from the probe surface to the fluid and is ultimately the one absorbed by the cooled cell wall. The total heat transfer area $A_s = \pi DL =$ (D is the probe diameter); the energy balance gives

$$\dot{Q} = hA_s\Delta T_\infty \implies h = \frac{\dot{Q}}{\pi DL\Delta T_\infty} \quad (9)$$

where $\Delta T_\infty = T_{probe} - T_{ref}$ is the steady temperature difference between the probe surface and the cell internal wall. The latter is detected by a thermocouple located on the wall. The plateau duration is identified on the ΔT vs. ln t curve as the region at the end of the test with nearly zero slope; using the average temperature in this region, the natural-convection coefficient h around a slender vertical cylinder is obtained.

3.2. Method and Device Description

The experimental evaluation of the thermal conductivity and convection heat transfer coefficient of the developed aluminum cellular structure was carried out using the thermal conductivity probe (TCP) method [25,26], used by the authors as a standard method [27–29]. The probe is one of the thermal probes built in their laboratory. The probe used in the present work was 60 mm long and 0.6 mm in diameter; the resulting length-to-diameter ratio was about 100, ideal to approximate an infinite-length wire [26]. The TCP was an AISI316 stainless-steel tube with a platinum heating wire and a K-type thermocouple inserted in it. The rest of cavity as filled with a low-viscosity epoxy resin. Thus, it made it easy to identify the linear portion of the ΔT–ln t curve of the temperature increase. Due to its slender shape (Figure 5), the probe could be easily inserted into the voids of the metal cellular structure, without the need to alter its morphology.

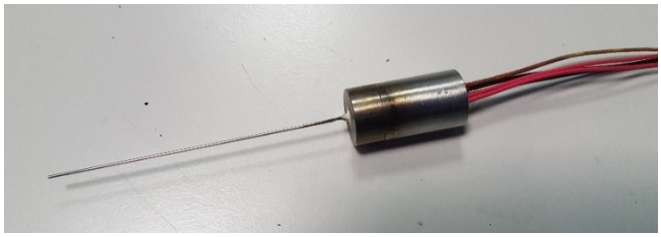

Figure 5. Picture of the probe, from [27].

The test setup (Figure 6) was made of a glass measurement cell, a stabilized power supply, a data acquisition system (DAS) for continuous signal recording, a thermostat to regulate the temperature of the thermostatic fluid, and an ice Dewar acting as a cold junction for the thermocouples. This configuration allowed testing in both air and water and ensured controlled conditions.

3.3. Test Procedure

Once the sample and probe are mounted in the cell and the cell filled with the test fluid (pure distilled water or air), the thermostatic fluid (water added with ethylene glycol) circulates around the cell until the desired test temperature is reached and stabilized. When thermal equilibrium is achieved, the heating current is switched on and applied to the probe. Different currents are supplied as a function of the working fluid and the desired maximum temperature to be reached, according to the Table 3.

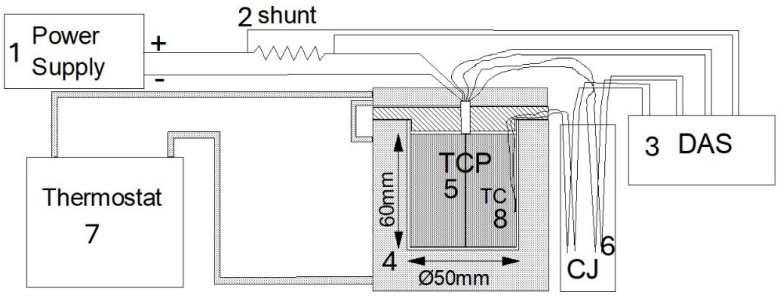

Figure 6. Sketch of the experimental apparatus with its components: 1—stabilized power supply; 2—0.1 Ω shunt; 3—DAS: data acquisition system; 4—measuring cell, made of a glass container, a glass cover, thermostatic fluid (water + ethylene glycol), and TCP (5), vertically positioned, is contained; 6—CJ: Dewar with mashed ice, acting as cold junction for the thermocouples; 7—thermostat supplying the thermostatic fluid; 8—TC, internal cell wall thermocouple. From [27].

Table 3. Test temperatures and heating currents applied during the experimental measurements in air and water using the thermal conductivity probe.

Fluid	Test Temperatures (°C)	Heating Current (mA)
Air	5, 20, 40	50, 75, 100, 125, 150
Water		150, 200, 250, 300, 350

Lower currents are sufficient for air, while higher currents are needed in water to compensate for its greater heat capacity, thermal conductivity, and convection heat transfer coefficient. During measurements, the probe and wall temperatures, the shunt voltage drop, and the platinum heater voltage drop were continuously recorded by the DAS. Acquired data were processed, first plotting the probe temperature rise as a function of the logarithm of time, then identifying the linear segment of this trend and evaluating its slope m. The thermal conductivity of the tested sample as calculated through Equation (7) [24].

When free convection in the fluid (located interstitially in the sample) starts, corresponding to the heat transferred from the probe to the cell wall in the steady state, the convection heat transfer coefficient is calculated from the temperature difference between the probe and the wall (Equation (9)). Figures 7 and 8 show the typical trends in the temperature rise versus the logarithm of time for the aluminum cellular structure tested in air and water, respectively. In these figures, the linear ΔT region for determining λ and the constant region for evaluating h are outlined, respectively, as reported in Table 4.

Table 4. Time intervals of the linear portion (for estimating λ) and the constant ΔT region (for calculating h) in both air and water.

	Time (Start and End)	
	Air	Water
Linear portion	4.5 s–33 s	7.4 s–55 s
Constant ΔT	90 s–2980 s	403 s–1808 s

These trends correspond to the typical thermal responses of the probe when measuring porous materials saturated with fluids. For both fluids, an initial curved region due to heat capacity, then a linear portion, and finally a constant temperature due to convection are clearly recognizable in Figures 7 and 8.

The fitting line of the linear trend in Figure 8 (for instance) is reported in Figure 9 for the range used for λ determination.

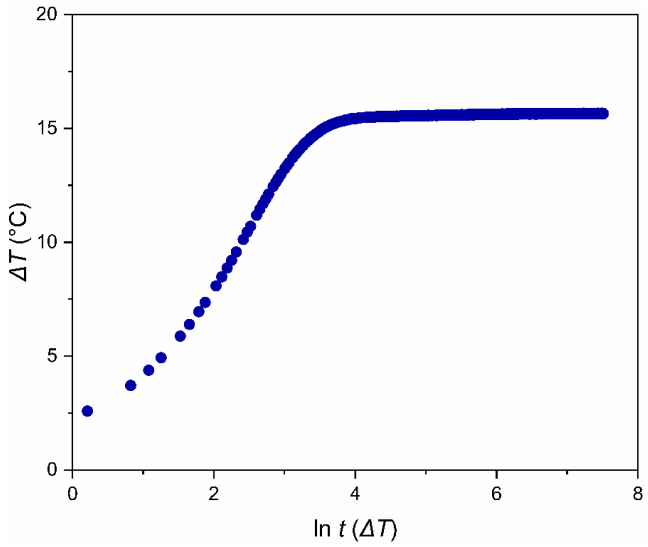

Figure 7. Typical trend in temperature increase vs. logarithm of time in air.

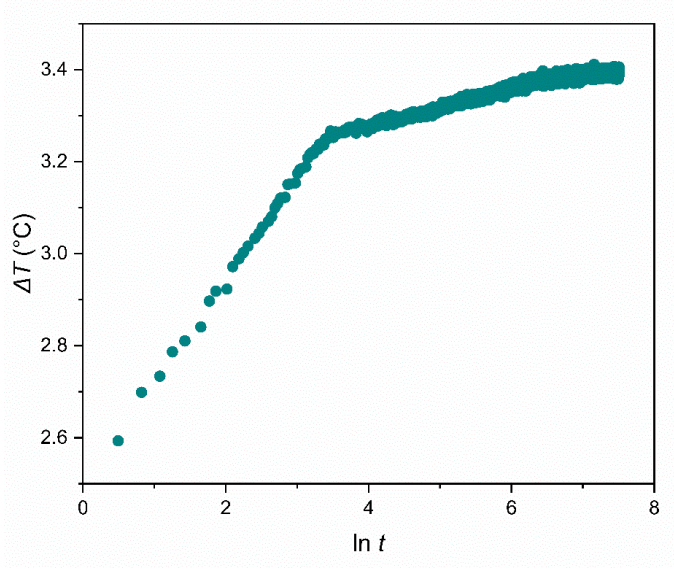

Figure 8. Typical trend in the temperature increase vs. the logarithm of time in water.

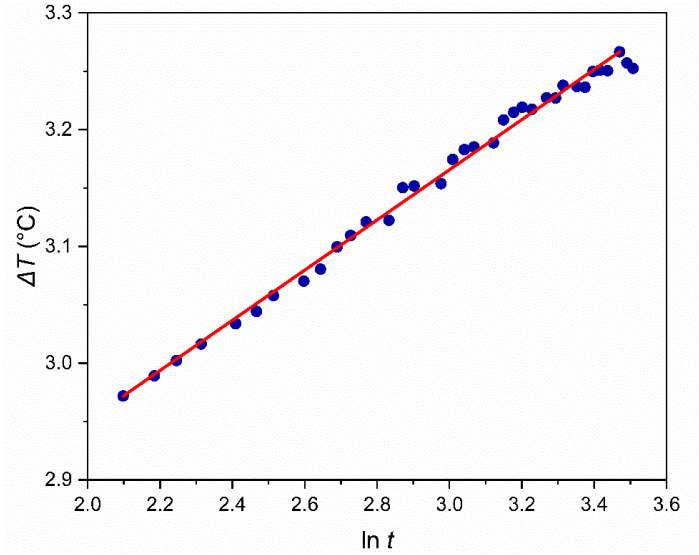

Figure 9. Portion of ΔT vs. ln t trend in Figure 8, clearly verifying the linear behavior and the straight regression line.

4. Results

4.1. Thermal Conductivity

The results of all tests carried out are shown in Figures 10 and 11 for air and water, respectively, as a function of the average test temperature. Both figures show a clear increasing trend, indicating that the thermal conductivity of the aluminum cellular structure progressively increases with temperature.

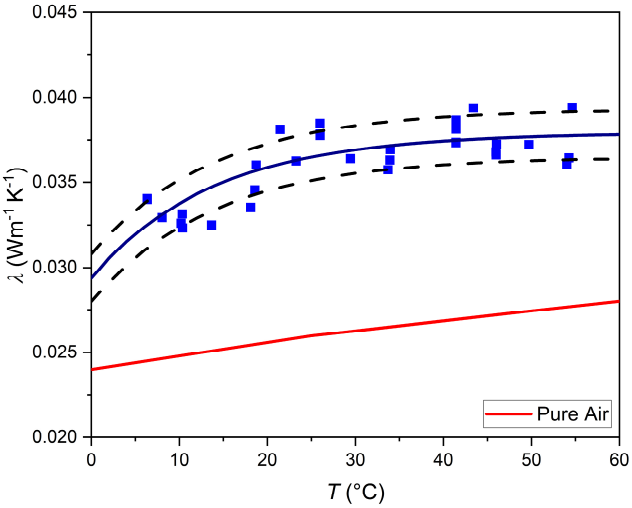

Figure 10. Measured thermal conductivity (λ) of the aluminum cellular structure in air as a function of temperature in comparison with pure air (red line) in the literature [30]. The blue dots are the experimental data. Dashed black lines are the ±1 σ confidence bands (approximately 68% of the data).

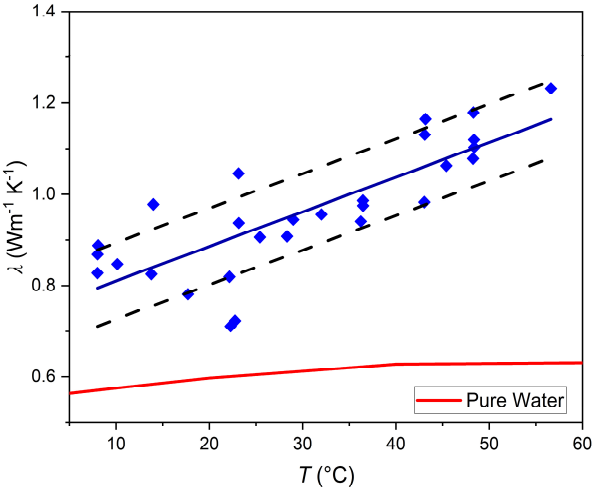

Figure 11. Measured thermal conductivity (λ) of the aluminum cellular structure in water at different temperatures. The definition of the lines is the same as that in Figure 10. Comparison with pure water data from the literature [30].

In air (Figure 10), λ ranges from approximately 0.034 W m^{-1} K^{-1} at low temperatures to about 0.038 W m^{-1} K^{-1} at higher temperatures. Compared with pure air (λ = 0.025 ÷ 0.027 W m^{-1} K^{-1}, from the literature [30], also shown in Figure 10), the cellular structure exhibits an enhancement in λ of approximately 37–45%, depending on temperature. The corresponding quantitative values and percentage improvements are summarized in Table 5. This behavior is attributed to the presence of the solid metallic skeleton, which provides preferential conduction paths through the structure. At temperatures above about 40 °C, λ tends to stabilize, showing only minor variations.

Table 5. Comparison of λ for air and water, measured for the pure fluids and for the fluid–cellular structure configuration at representative temperatures (5, 20, and 40 °C). The percentage improvement is computed as $\left(\lambda_{fluid+structure} - \lambda_{fluid}\right)/\lambda_{fluid} \times 100$.

T (°C)	λ_{air} (W m^{-1} K^{-1})	$\lambda_{air+structure}$ (W m^{-1} K^{-1})	$\Delta\lambda_{air}$ (%)	λ_{water} (W m^{-1} K^{-1})	$\lambda_{water+structure}$ (W m^{-1} K^{-1})	$\Delta\lambda_{water}$ (%)
5	0.0245	0.0336	37.1	0.563	0.817	45.1
20	0.0257	0.0373	45.1	0.597	0.950	59.1
40	0.0272	0.0376	38.2	0.628	1.126	79.3

In water (Figure 11), no significant change in slope is observed, and λ increases about 50% (from approximately 0.8 W m^{-1} K^{-1} to 1.2 W m^{-1} K^{-1}) as temperature rises. Compared to pure water (from literature [30], shown in Figure 11 as a continuous line), the cellular structure leads to an enhancement ranging from about 45% to 80%, depending on the temperature. The corresponding quantitative values and percentage improvements are summarized in Table 6.

Table 6. Comparison of convection heat transfer coefficient for air and water, measured for the pure fluids and for the fluid–cellular structure configuration at representative temperatures (5, 20, and 40 °C). The percentage improvement is computed as $\left(h_{fluid+structure} - h_{fluid}\right)/h_{fluid} \times 100$.

T (°C)	h_{air} (W m^{-2} K^{-1})	$h_{air+structure}$ (W m^{-2} K^{-1})	Δh_{air} (%)	h_{water} (W m^{-2} K^{-1})	$h_{water+structure}$ (W m^{-2} K^{-1})	Δh_{water} (%)
5	30.9	37.8	22.0	240.7	369.8	53.7
20	30.4	39.0	28.3	340.7	406.7	19.7
40	31.2	41.0	31.6	370.8	439.9	18.6

The quantitative improvement ratios of λ at the selected temperature points (5, 20, and 40 °C) are summarized in Table 5.

4.2. Convection Heat Transfer Coefficient

The experimental analysis of the convection heat transfer coefficient also confirms the increase in this coefficient when the structure is present.

In air (Figure 12), the measured h ranges between approximately 37.8 and 41.0 W m^{-2} K^{-1} over the investigated temperature range, showing a slight but clear increase in h with temperature. This behavior indicates that the tested cellular structure does not significantly hinder air circulation but generates a stable convective flow pattern within the pores.

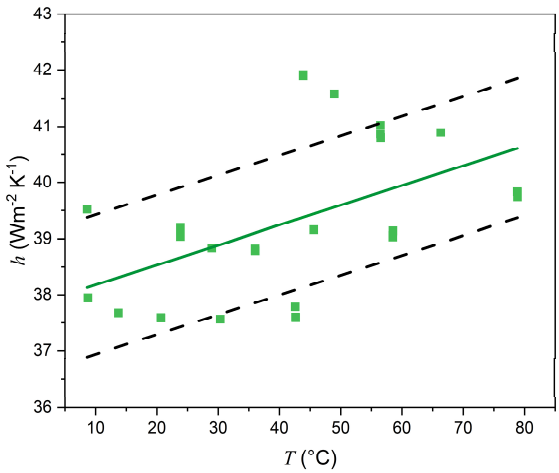

Figure 12. Convection heat transfer coefficient (h) of the aluminum cellular structure in air. The green dots are the experimental data. Dashed black lines are the ±1 σ confidence bands (approximately 68% of the data).

In water (Figure 13), the convection heat transfer coefficient is much higher, ranging from approximately 370 to over 440 W m^{-2} K^{-1}, with a nearly linear increase with temperature. The results reported in Figures 12 and 13 indicate that the metallic cellular structure does not hinder the onset of free convection and may locally enhance the heat transfer within the pores. Similar trends were also observed in [29] for a different medium (spherical olivine particles in air and water).

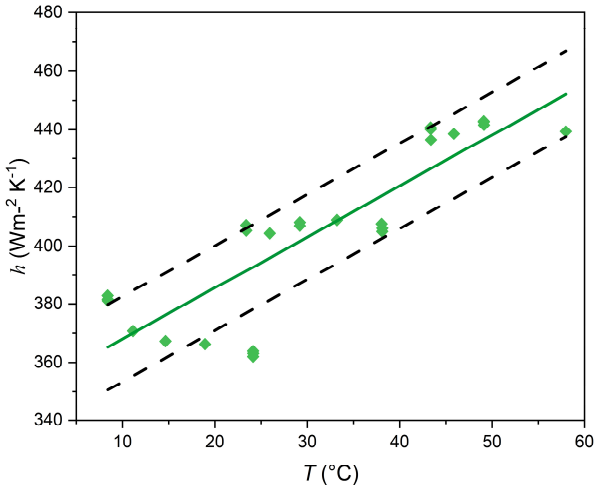

Figure 13. Convection heat transfer coefficient (*h*) of the aluminum cellular structure in water. The definition of the lines is the same as that in Figure 12.

To quantitatively assess the effect of the cellular structure on convection heat transfer, the experimentally obtained values were compared with direct measurements carried out with pure fluids. The results are presented in Figures 14 and 15 for air and water, respectively. The comparison is based on the experimental regressions previously obtained and reported in Figures 12 and 13. The average values of the convection heat transfer coefficient used as reference in Figure 14 (air) and Figure 15 (water) were extracted from the corresponding continuous regression lines shown in Figures 12 and 13, respectively. Pure fluids were tested following the same procedure adopted for the structures, with the TCP vertically aligned at the center of the measuring cell. Due to the very thin shape of the probe, no wall effects were observed, and negligible temperature differences were detected between the probe's outer surface and the surrounding structure. For air (Figure 14), the presence of the cellular structure increases *h* by approximately 22–32%, with the enhancement slightly increasing with temperature, as reported in Table 5. For water (Figure 15), larger improvements in *h* are observed at low temperatures (≈54% at 5 °C), while the enhancement decreases to about 19% at higher temperatures (Table 6).

The quantitative improvement ratios of *h* at the selected temperature points (5, 20, and 40 °C) are summarized in Table 6.

Similar data were reported in [27], which were obtained with the same procedure on a different cellular structure and show that *h* increases when the material is highly conductive (aluminum alloy), whereas it remains nearly constant for an insulating material (PLA). Therefore, the observed enhancement in *h* is mainly attributable to heat conduction through the solid phase.

Overall, the comparisons confirm that the adoption of a metal cellular structure effectively improves both conduction and convection heat transfer compared to pure fluids, demonstrating

- The validity of the adopted measuring procedure;
- The potential of these structures for designing thermal management systems when high heat transfer is required.

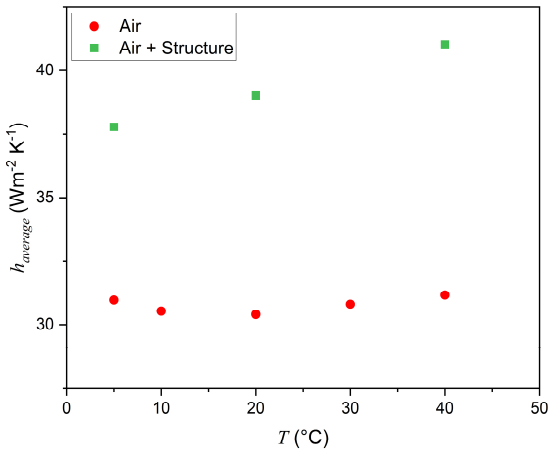

Figure 14. Comparison of the average convection heat transfer coefficient (h_{average}) between pure air and air for the aluminum cellular structure as a function of temperature.

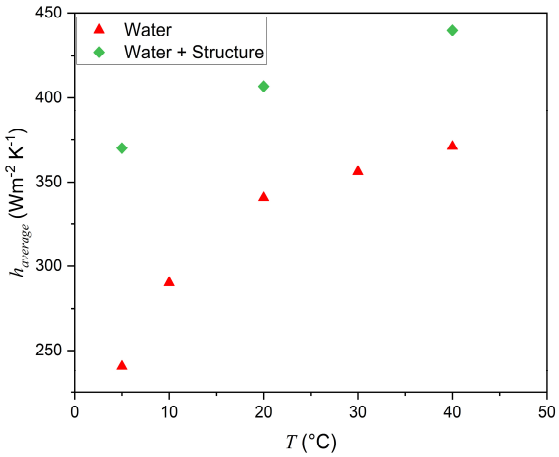

Figure 15. Comparison of measured values of the convection heat transfer coefficient (h) between pure water and water for the aluminum cellular structure as a function of temperature.

5. Uncertainty Analysis

An uncertainty estimation was performed according to the ISO GUM guidelines [31], considering both type A (statistic) and type B (non-statistic) as components.

Thermal conductivity:

The type A component is derived from the spread of repeated measurements and the regression for slope estimation. It resulted negligible compared to the type B sources.

The type B component includes the calibration of the probe and thermocouples, with an estimated uncertainty of about ±4% [25]. Repeatability of the thermocouple values (~±0.3 °C) is already included in calibration uncertainty, and is considered negligible. Overall, the λ uncertainty is estimated at about ±5%.

Convection heat transfer coefficient:

Being the relative uncertainty of h calculated from its defining equation:

$$h = \frac{\dot{Q}}{A\Delta T} = \frac{RI^2}{2DL\Delta T} \tag{10}$$

The relative standard deviation assumes the value:

$$\frac{\sigma_h}{h} = \sqrt{\left(\frac{\sigma_R}{R}\right)^2 + \left(2\frac{\sigma_I}{I}\right)^2 + \left(\frac{\sigma_A}{A}\right)^2 + \left(\frac{\sigma_{\Delta T}}{\Delta T}\right)^2} \tag{11}$$

For instance, a typical test (λ measurement in air, with $I = 50$ mA, $T = 5$ °C, $R = 6.5$ Ω) supplies $\frac{\sigma_R}{R} = 0.05\%$, $\frac{\sigma_I}{I} = 0.007\%$, $\frac{\sigma_{\Delta T}}{\Delta T} = 0.2\%$, and $\frac{\sigma_A}{A} = 0.08\%$, leading to a total uncertainty $\frac{\sigma_h}{h} = 0.22\%$.

Among these terms, the contribution due to ΔT is the largest. However, this theoretical calculation tends to underestimate the real uncertainty because it does not account for the inherent variability in free convection due to the generation of fluid convective cells, in of ambient conditions, or presence of internal obstacles, in summary, the random motion of fluids in the structure. For this reason, the total uncertainty for h is prudently estimated at 15–20%, consistent with the literature [32].

6. Conclusions

The present study demonstrates the effectiveness of the "Lost-PLA" process as a technique for manufacturing complex metallic cellular structures with aluminum alloy. The integration of parametric CAD modeling enables the generation of optimized, repetitive, and easily adjustable geometries, providing significant design flexibility. The experimental analysis shows that the quality of the polymer model produced by 3D printing is crucial for ensuring the dimensional accuracy and successful execution of samples during the burnout and casting stages.

The experimental results obtained using the thermal conductivity probe method clearly show that inserting a porous aluminum alloy structure into a fluid medium, such as air or water, significantly improves both the thermal conductivity and convection heat transfer coefficient compared to pure fluid. Quantitatively, the effective thermal conductivity increased by approximately 37–45% in air and 45–80% in water, while the convective heat transfer coefficient improved by about 22–32% in air and 19–54% in water, depending on the temperature. In particular, the increase in λ highlights the "thermal bridges" provided by the metal matrix, while the increase in h confirms that the cellular structure does not hinder natural convection but instead enhances it by promoting the local heat transfer mechanisms within the pores and a larger exchange surface. The differences observed between air and water also confirm that this effect is more pronounced in fluids with higher heat capacity. These findings indicate the strong potential of cellular metallic structures as innovative materials for lightweight heat exchangers, thermal storage units, or advanced cooling systems where low weight, high specific surface area, and good heat transfer properties are required.

Finally, the measurement procedure has proved to be reliable, provided that the uncertainties related to natural convection phenomena are carefully evaluated and taken into account, with instrumental errors remaining small compared to the intrinsic variability in buoyancy-driven convection.

The results obtained open interesting perspectives for applying this methodology in engineering fields where lightweight structures, high thermal performance, and customizable geometries are required. Future developments could include further optimizing process parameters and investigating alternative cell configurations to further expand the potential of this approach.

Author Contributions: Conceptualization, P.C. and S.C.; methodology, A.C., P.C., S.C., G.C. and M.E.T.; software, A.C. and P.C.; formal analysis, A.C., P.C. and S.C.; investigation, A.C., P.C., S.C., G.C. and M.E.T.; data curation, A.C., P.C. and S.C.; writing—original draft preparation, A.C., P.C., S.C., G.C. and M.E.T.; writing—review and editing, A.C., P.C., S.C., G.C. and M.E.T. All authors have read and agreed to the published version of the manuscript.

Funding: This research received no external funding.

Institutional Review Board Statement: Not applicable.

Informed Consent Statement: Not applicable.

Data Availability Statement: The data presented in this paper are available on request from the corresponding author.

Acknowledgments: The authors thank Piero Plini and Benedetto Iacovone for their technical support and assistance with experiments.

Conflicts of Interest: The authors declare no conflicts of interest.

Abbreviations

Latin	
A_s	*External Surface Area of Probe* (m^2)
D	*Probe Diameter* (m)
d_p	*Pore Diameter* (m)
d_s	*Structure Diameter* (m)
H_b	*Basement Height* (m)
H_s	*Structure Height* (m)
h	*Convection Heat Transfer Coefficient* ($W\ m^{-2}\ K^{-1}$)
I	*Electric Current* (A)
L	*Probe Length* (m)
m	*Mass* (kg)
$\dot{Q}$	*Thermal Power* (W)
$\dot{q}$	*Thermal Power per Unit Length* ($W\ m^{-1}$)
R	*Electric Resistance* (Ω)
r	*Cylinder Radius* (m)
T	*Temperature* (°C)
t	*Time* (S)
V_{ext}	*External Volume of Cellular Structure* (mm^3)
Greek	
α	*Thermal Diffusivity* ($m^2\ s^{-1}$)
Δ	*Difference*
λ	*Thermal Conductivity* ($Wm^{-1}\ K^{-1}$)
ρ^*	*Apparent Density* ($kg\ m^{-3}$)
ρ_s	*Solid Density* ($kg\ m^{-3}$)
σ	*Standard Deviation*
ϕ	*Porosity*
Geometrical symbols	
$\varnothing_s$	*Structure Diameter* (m)
$\varnothing_b$	*Basement Diameter* (m)
Acronyms	
CAD	Computer Aided Design
CFD	Computational Fluid Dynamics
DAS	Data acquisition System
PLA	Poly Lactic Acid
STL	Stereolithography
TCP	Thermal Conductivity Probe
TPMS	Triply Periodic Minimal Surfaces

References

1. Lu, T.J.; Stone, H.A.; Ashby, M.F. Heat Transfer in Open-Cell Metal Foams. *Acta Mater.* **1998**, *46*, 3619–3635. [CrossRef]
2. Calmidi, V.V.; Mahajan, R.L. Forced Convection in High Porosity Metal Foams. *J. Heat Transf.* **2000**, *122*, 557–565. [CrossRef]
3. Boomsma, K.; Poulikakos, D. On the Effective Thermal Conductivity of a Three-Dimensionally Structured Fluid-Saturated Metal Foam. *Int. J. Heat Mass Transf.* **2001**, *44*, 827–836. [CrossRef]

4. Jin, L. Forced Convection Heat Transfer in a Porous Channel Subjected to Oscillating Flow. Ph.D. Thesis, Nanyang Technological University, Singapore, 2006.
5. Mancin, S.; Zilio, C.; Rossetto, L.; Cavallini, A. Heat Transfer Performance of Aluminum Foams. *J. Heat Transf.* **2011**, *133*, 060904. [CrossRef]
6. Nawaz, K.; Bock, J.; Jacobi, A.M. Thermal-Hydraulic Performance of Metal Foam Heat Exchangers under Dry Operating Conditions. *Appl. Therm. Eng.* **2017**, *119*, 222–232. [CrossRef]
7. Bayomy, A.M.; Saghir, Z. Experimental and Numerical Study of the Heat Transfer Characteristics of Aluminium Metal Foam (with/without Channels) Subjected to Steady Water Flow. *Pertanika J. Sci. Technol.* **2016**, *25*, 221–246.
8. Chen, K.; Guo, L.; Wang, H. A Review on Thermal Application of Metal Foam. *Sci. China Technol. Sci.* **2020**, *63*, 2469–2490. [CrossRef]
9. Xiao, T.; Lu, L.; Peng, W.; Yue, Z.; Yang, X.; Lu, T.J.; Sundén, B. Numerical Study of Heat Transfer and Load-Bearing Performances of Corrugated Sandwich Structure with Open-Cell Metal Foam. *Int. J. Heat Mass Transf.* **2023**, *215*, 124517. [CrossRef]
10. Su, X.; Zhang, Y.; Rao, Y.; Yeranee, K.; Wang, X. Experimental and Numerical Study on Flow and Heat Transfer Characteristics of Additively Manufactured Triply Periodic Minimal Surface (TPMS) Heat Exchangers for Micro Gas Turbine. *Aerospace* **2025**, *12*, 416. [CrossRef]
11. Liu, J.; Cheng, D.; Oo, K.; McCrimmon, T.L.; Bai, S. Design and Additive Manufacturing of TPMS Heat Exchangers. *Appl. Sci.* **2024**, *14*, 3970. [CrossRef]
12. Pan, C.; Han, Y.; Lu, J. Design and Optimization of Lattice Structures: A Review. *Appl. Sci.* **2020**, *10*, 6374. [CrossRef]
13. Kim, J.; Yoo, D.-J. 3D Printed Compact Heat Exchangers with Mathematically Defined Core Structures. *J. Comput. Des. Eng.* **2020**, *7*, 527–550. [CrossRef]
14. Maskery, I.; Sturm, L.; Aremu, A.O.; Panesar, A.; Williams, C.B.; Tuck, C.J.; Wildman, R.D.; Ashcroft, I.A.; Hague, R.J.M. Insights into the Mechanical Properties of Several Triply Periodic Minimal Surface Lattice Structures Made by Polymer Additive Manufacturing. *Polymer* **2018**, *152*, 62–71. [CrossRef]
15. Mahjoob, S.; Vafai, K. A Synthesis of Fluid and Thermal Transport Models for Metal Foam Heat Exchangers. *Int. J. Heat Mass Transf.* **2008**, *51*, 3701–3711. [CrossRef]
16. Gangapatnam, P.; Kurian, R.; Venkateshan, S.P. Numerical simulation of heat transfer in metal foams. *Heat Mass Transfer* **2018**, *54*, 553–562. [CrossRef]
17. Yan, H.; Fang, K.; Wu, W.T.; Zhao, Z.; Feng, F. Thermal performance enhancement by modifying the spiral flow and turbulence transport in an X-lattice cellular structure. *Int. J. Therm. Sci.* **2024**, *205*, 109277. [CrossRef]
18. Aider, Y.; Singh, P. Experimental Study on Flow and Thermal Transport in Additively Manufactured Architectured Lattice Frame with Air and Particles as Convective Agents. *J. Therm. Sci. Eng. Appl.* **2025**, *17*, 051006. [CrossRef]
19. Li, Y.; Niu, Z.; Gao, X.; Guo, J.; Yang, X.; He, Y.-L. Effect of Filling Height of Metal Foam on Improving Energy Storage for a Thermal Storage Tank. *Appl. Therm. Eng.* **2023**, *229*, 120584. [CrossRef]
20. Kang, D.G.; Lee, D.K.; Choi, J.M.; Shin, D.K.; Kim, M.S. Study on the Metal Foam Flow Field with Porosity Gradient in the Polymer Electrolyte Membrane Fuel Cell. *Renew. Energy* **2020**, *156*, 931–941. [CrossRef]
21. Ceci, A.; Costanza, G.; Savi, G.; Tata, M.E. Optimization of the Lost PLA Production Process for the Manufacturing of Al-Alloy Porous Structures: Recent Developments, Macrostructural and Microstructural Analysis. *Int. J. Lightweight Mater. Manuf.* **2024**, *7*, 662–667. [CrossRef]
22. Tao, W.; Leu, M.C. Design of Lattice Structure for Additive Manufacturing. In *Proceedings of the 2016 International Symposium on Flexible Automation (ISFA)*; IEEE: Cleveland, OH, USA, 2016; pp. 325–332.
23. Gibson, L.J.; Editor, G. Cellular Solid. *MRS Bull.* **2003**, *28*, 270–274. [CrossRef]
24. Carslaw, H.S.; Jaeger, J.C. *Conduction of Heat in Solids*, 2nd ed.; Clarendon Press: Oxford, UK, 1959.
25. Wechsler, A.E. The Probe Method for Measurement of Thermal Conductivity. In *Compendium of Thermophysical Property Measurement Methods: Volume 2 Recommended Measurement Techniques and Practices*; Maglić, K.D., Cezairliyan, A., Peletsky, V.E., Eds.; Springer: Boston, MA, USA, 1992; pp. 161–185, ISBN 978-1-4615-3286-6.
26. *ASTM D5334-14*; Standard Test Method for Determination of Thermal Conductivity of Soil and Soft Rock by Thermal Needle Probe Procedure. ASTM International: West Conshohocken, PA, USA, 2014.
27. Bovesecchi, G.; Coppa, P.; Corasaniti, S.; Costanza, G.; Potenza, M.; Tata, M.E. Experimental Tests of Conduction/Convection Heat Transfer in Very High Porosity Foams with Lattice Structures, Immersed in Different Fluids. *Energies* **2023**, *16*, 5959. [CrossRef]
28. Barbero, F.; Verona Rinati, G.; Bovesecchi, G.; Corasaniti, S.; Potenza, M.; Coppa, P.; Pisano, C. Analysis of the ice front propagation in heart tissues: First results. *Int. J. Therm. Sci.* **2024**, *205*, 109289. [CrossRef]
29. Corasaniti, S.; Gori, F. Natural Convection Around a Vertical Cylinder (thermal probe) Immersed in a Porous Medium. *Int. Comm. Heat Mass Transf.* **2017**, *81*, 72–78. [CrossRef]
30. Beaton, C.F.; Hewitt, G.F. *Physical Properties Data for the Design Engineer*; Hemisphere Publishing Corporation: London, UK, 1989; ISBN 0-89116-739-0.

31. *ISO-IEC 98-3:2008*; Uncertainty of Measurement—Part 3: Guide to the Expression of Uncertainty in Measurement (GUM:1995). ISO: Geneva, Switzerland, 2008.
32. Eckert, E.R.G.; Drake, R.M. *Heat and Mass Transfer*, 10th ed.; Mc Graw Hill: New York, NY, USA, 1959.

Disclaimer/Publisher's Note: The statements, opinions and data contained in all publications are solely those of the individual author(s) and contributor(s) and not of MDPI and/or the editor(s). MDPI and/or the editor(s) disclaim responsibility for any injury to people or property resulting from any ideas, methods, instructions or products referred to in the content.